Microgrid energy management strategies assessment through coupled thermal-electric considerations

Spyridon Chapaloglou[a], Athanasios Nesiadis[b], Konstantinos Atsonios[b], Nikos Nikolopoulos[b], Panagiotis Grammelis[b], Angel Carrera[c], Oscar Camara[c]

[a] *Department of Electric Power Engineering, Norwegian University of Science and Technology, Trondheim, Norway, spyridon.chapaloglou@ntnu.no*
[b] *Centre for Research & Technology Hellas /Chemical Process and Energy Resources Institute, Thessaloniki, Greece, nesiadis@certh.gr, atsonios@certh.gr, n.nikolopoulos@certh.gr, grammelis@certh.gr*
[c] *Aiguasol Enginyeria, Barcelona, Spain, angel.carrera@aiguasol.coop, oscar.camara@aiguasol.coop*

Abstract:
Battery Energy Storage Systems (BESSs) are considered as one of the most promising technological options towards high self-sufficiency of building facilities and higher independency from the main grid through autonomous operation. At the same time, BESS are an essential component for a cost-optimized operation of grid-connected microgrids. In addition, the ever-increasing trend to replace conventional heating systems with electrically driven heat pumps, reveals a continuously emerging trend for electrification supported by electrical storage systems. In this study, a grid-connected microgrid of a sport centre facility located in Barcelona (Spain), which includes i) a solar PV (Photovoltaic) installation, ii) a BESS and iii) a heat pump (HP), is investigated through dynamic simulations, considering both thermal and electrical loads. Targeting the best compromise between self-sufficiency and reduction in the cost of electricity, two different energy management strategies are examined for the supervision and control of the grid-connected microgrid operation, taking into account the impact of the already operating HVAC (Heating Ventilation and Air Conditioning) systems along with the HP operation. In particular, the investigated energy management strategies are considered to be two of the most prominent ones and involve 1) peak shaving of the microgrid consumption with off-peak grid power and 2) pricing-based operation of the BESS (arbitrage), according to the main grid electricity price. Under this scope, an integrated thermal and electrical dynamic model of the sport centre energy system is developed in APROS software. The results are benchmarked against the corresponding ones from the standard model of TRNSYS. The impact of each management strategy is assessed in terms of the resulting power flows and the associated cost of electricity, for each operational mode. Based on the simulation results, the most advantageous energy management algorithm is determined for each case study, revealing that the integrated thermal-electrical dynamic modelling can be a useful tool for designing adaptive energy management algorithms.

Keywords: Battery Energy Storage; heat pump; energy management; dynamic simulation; APROS; TRNSYS

1. Introduction

Heating sector is considered among the most energy demanding sectors and responsible for more than 25% of the CO_2 emissions globally, making the decarbonisation of the heating and cooling necessary for the drastic reduction of GHG (Greenhouse Gas) emissions. It is estimated that the supply of electricity, gas, steam and air conditioning have by far the highest GHG intensity and carbon footprint in the EU-28 (European Union) whereas private households are the biggest contributors (25%) to total emissions of ozone precursors [1]. More specifically, in EU-28 the main use of energy by the residential sector (64.1% of final energy consumption) is related to building heating, while together with the hot water demand this can reach up to 78.9% of the final energy consumption [1]. For the particular building type of sport centres, this trend is even more intense as the total heating demand is 3-5 times greater than the electricity demand [2]. This is attributed to the several heat demanding facilities typically found in such places (sport halls, changing rooms, swimming pools) requiring both temperature regulation and air quality improvement. Therefore, sport centres are among the highest energy consuming building types, especially in cases were swimming pools facilities are present [3]. Therefore it is evident that there is a great environmental potential benefit in improving sport centres energy consumption efficiency and this can further be an important contribution towards the achievement of EU's Climate and

Energy Framework goals for 2030 (40% emissions reduction) [1]. One of the most anticipated strategies to achieve this goal, is the electrification of the heating and cooling systems by utilizing HPs in combination with RES (Renewable Energy Sources). In this study, such a case is presented, where the heat and electricity demand of a sport centre (with swimming pool facilities) are simultaneously addressed. Two different EMS (Energy Management System) strategies are implemented in the integrated thermal-electrical system and reveal additional benefits of the proposed configuration in terms of operational costs reduction.

1.1 Recent advances on heat pump modelling, integration of them in microgrids and EMS strategies

Many studies have been reported during the previous years regarding the development of HP models either for design purposes or for operation optimization. In studies such as in [4], [5], [6] [7], where the main purpose is the energy system modelling (heating system and HVAC), a common approach for the dynamic simulation of the HP is the implementation of a performance map. This is basically a look-up table description of the HP performance which correlates the electrical power supply with a specific heat output. These types of data are possible to be provided by the manufacturer. Studies similar to the aforementioned ones are usually implemented in TRNSYS software, where it is possible to integrate various HVAC systems into a single system-level simulation. For such thermal system design studies, a simple static mathematical model based on the performance map of the HP could be enough. However, for the investigation of the HP performance under varying environmental conditions and thermal loads, a higher fidelity dynamic approach is necessary. Such a dynamic model could be based either on first principles modelling (fundamental physics equations) or on data assimilation techniques, if operational data are available from the manufacturer. This was the case in [8], where a detailed dynamic model of an air-to-water HP with a screw compressor that was validated against experimental data is presented. The increase of the level of detail in HP modelling also gives the opportunity to include various control systems that aim to stabilize the system and achieve the desired performance in the most efficient way. Under this scope, various control configurations can be tested and tuned before the real system application. In [9], a detailed HP dynamic model with its corresponding control structures was developed in Dymola and the system was simulated for two different refrigerants (R744, R410A). In [10], an air-source HP was also modelled in Dymola and an Extremum Seeking Algorithm (ESC) was employed for the control of the system. The authors reported that this model-free proposed self-optimizing methodology performed better compared to model based control design. In [11], a new methodology was introduced for the control of a HP in cooling mode, based on evaporator outlet pressure reading, while in [12] the modelling, optimization and optimal control of a transcritical CO_2 HP with thermal storage system, developed in Dymola, was examined. In [13], a genetic algorithm and a feedforward ANN were employed for the optimization of heating and cooling performances of an air source HP, considering the availability of design and operating data. In [14], the coupling of TRNSYS and EES was employed to demonstrate a capacity-controlled ground source HP. In [15], three different control methodologies (PID, ANN, Fuzzy) for the control of a Variable Speed Compressor (VSC) and Electronic Expansion Valve (EEV) were compared and the ANN was found to be the most effective, resulting in lower power consumption. It is worth noting that in most of the aforementioned studies as well as in [16] the two basic control elements in HP systems are i) the VSC and ii) the EEV or TXV (Thermal Expansion Valve).

Simultaneous use of variable speed compressors and expansion valves was discussed by [17] using a dual-Single Input –Single Output (SISO) strategy to regulate the compressor speed and refrigerant valve position in order to control the cooling capacity and evaporator superheating, respectively. Two separate proportional-integral (PI) feedback loops were devised in the proposed method. In [18], an air-source HP was modelled as a first order transfer function block and it was integrated into a microgrid simulation, while in [19] a variable speed HP was integrated into a power system simulation for frequency regulation.

There are many studies dedicated to the use of RES for HP power supply. In [20], authors demonstrated the ecological advantage of complementing the electric power input of an air source HP with solar and wind power. This benefit emerged from the low thermo-ecological cost compared to the cost occurring from HPs driven by electricity produced from non-renewable sources. In [21], a residential wind power driven HP was dynamically simulated based on simplified energy system models and was revealed that an energy storage system was necessary to be included in the overall heating system. It was also admitted that the augmentation of wind turbine capacity does not enhance the system autonomy, compared to the increase in the size of the storage system. In [22], a demand response scheme was implemented through the management and control of a

residential HP according to the dynamic electricity price and the level of the local photovoltaic power generation. These control strategies demonstrated possibilities for money savings and increased energy self-consumption. In [23], a grid connected HP combined with a heat storage tank system, capable of providing load flexibility upon grid request signals, was studied in terms of a dynamic exergoeconomic analysis, revealing that the operation according to the regulation request resulted in higher exergy destruction and higher overall cost of the system. In [24], a PV BESS system was modelled and it was found that the ratio of the installed PV peak power to the capacity of the battery had a significant influence on the self-consumption, autarky and economic self-sufficiency of the system. However, the authors claimed that a higher temporal resolution could affect the modelling results. In [25], the significance of BESS with different electricity tariff structures on revenue streams for existing PV system was investigated. It was revealed that the battery was preferably charged at the peak PV power generation and switch to grid charging when the PV power and the wholesale electricity price were low. The authors also highlighted the importance of a higher battery capacity which could result in a marginal increase in revenue. In [26], a new peak shaving algorithm was proposed for a PV BESS system based on a power balance set of rules strategy and dynamic minimum voltage tracking. Although the algorithm was tested and validated on a real time test bench, the authors pointed that a BESS utilization for peak shaving might not be always profitable. In [27], a PV BESS system for building-level applications was dynamically simulated and validated against experimental data. The BESS was controlled to provide the necessary power for the HVAC equipment based on two strategies, a) increase in PV self-consumption and b) grid peak shaving. It was proved that switching appropriately between the two strategies during the system operation, could reduce both contracted power and energy consumption for the examined case study. In [28], a hybrid PV/WT BESS system was dynamically simulated in TRNSYS for different uses (supermarket, offices, touristic centre, hotel), while a sensitivity analysis was carried out regarding the PV, WT and battery capacities. It was shown that hybrid systems are more effective in the case of more stable load profiles and a sensitivity analysis regarding the battery capacity is crucial to improve the profitability of the system, while for stand-alone systems the high components capital cost may not be balanced from the savings in operating costs. The authors also highlighted the significance of a more sophisticated simulation tool for the system designer in order to better estimate and optimize the components capacities.

1.2 Aim of the present study

As it is clear from the above analysis, addressing both thermal and electrical demands through coupled simulation can give deeper insights towards an optimized operation of the integrated energy systems. However, to the best of authors' knowledge, most of the studies lack a complete detailed modelling of all subsystems (thermal/electrical – consumption/generation) and most of them focus only on a particular operational strategy. Therefore, this study aims to compare and evaluate different energy management approaches for a microgrid operation, integrating detailed modelling for both thermal and electrical consumption and generation. Energy peak shaving and electricity price-based battery operation are compared on the basis of combined thermal-electrical system simulations. In this way, the power flows and the interaction between the various energy modules are revealed, while also highlighting the economic impact of the applied EMS strategies in conjunction with the system operation.

In this study, the case specific thermal demand associated to the usage patterns of a sport centre facilities is analysed, estimated and compensated from a HP, incorporating an appropriate control system design /enabled by its detailed numerical modelling (and validation with manufacturer data). Then, the HP's electrical consumption is coupled to the developed sport centre's electrical microgrid model (including detailed representations for the RES generation and the BESS) as a constant power load and the integrated thermal-electrical system is simulated under the supervisory management of the corresponding strategy. Finally, the results of the simulations of the under-investigation EMS strategies, are compared in terms of power flow analysis and cost of electricity reduction.

2 Integrated thermal-electrical modelling of the sport's centre energy systems

2.1 Modelling of the thermal energy systems and consumption in TRNSYS

The overall installation schematic is presented in Figure 1. The thermal loads can be grouped in four main sources, i.e. 1) building space heating and cooling, 2) DHW (Domestic Hot Water) preparation, 3) maintenance of the pool water temperature, 4) swimming pool hall. The thermal loads are supplied by a multipurpose HP

(capable of simultaneously or independently providing heating and cooling due to a source air heat exchanger capable of working either as evaporator or condenser) and a gas boiler, while air dehumidification is provided by the swimming pool AHU (Air Handling Unit), so they are in the last term covered by the electricity consumption of the HP and the AHU as well as the gas consumption of the boilers. Besides these two generation units, there are three distribution loops within the building: one for cooling and two for heating, one at a high temperature (80 ℃) and one at lower temperature (45 ℃). The high temperature loop is fed by the boiler and the low temperature loop mainly by the HP, but in case that the latter is not able to cope with the demand, the boiler also delivers the necessary power to the low temperature loop.

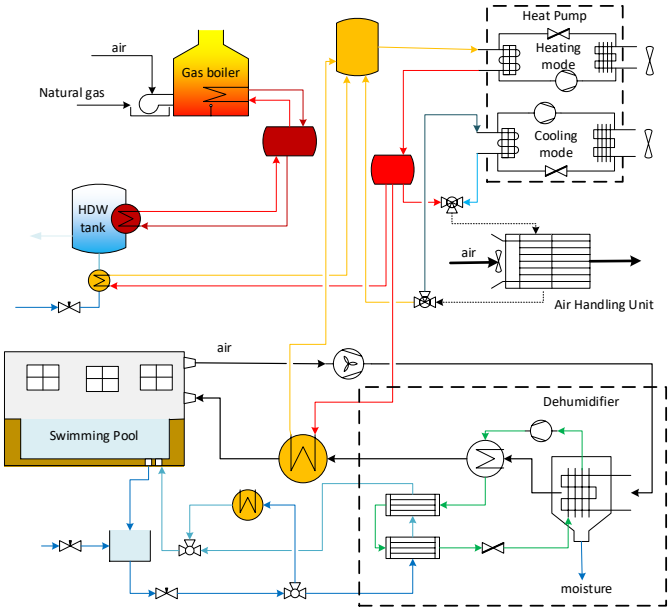

Figure 1: Sport centre's spaces-pool heating and DHW configuration.

The calculation of the space heating and cooling loads is done by means of the multi-zone building model in TRNSYS (known as type 56); nine thermal zones are defined within, according to the different uses and activities that take place in the building (see Figure 2). Energy rate control is used in all zones, except for the swimming pool hall zone where a temperature and humidity control is implemented, following the controls criteria in the operating AHU. This selection was done because the swimming pool hall has by far the highest thermal loads and a more accurate control was deemed necessary.

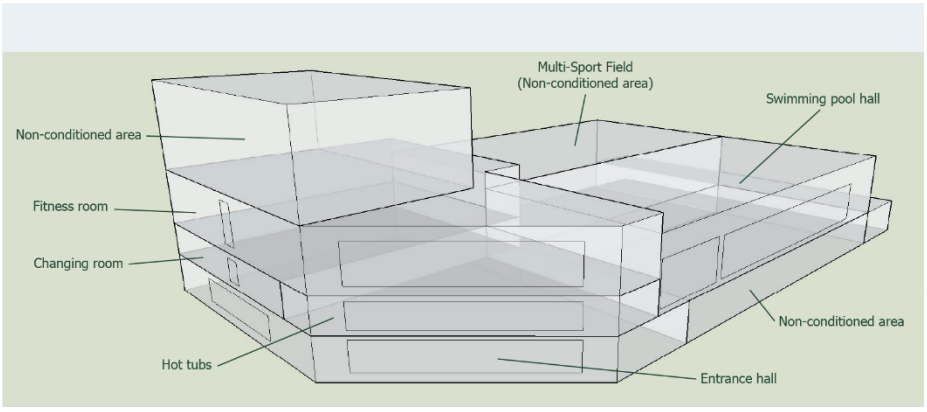

Figure 2: Sport centre's thermal zones modelled with TRNSYS.

The swimming pool model is a TRNSYS non-standard commercial, type 344, available from TRANSSOLAR. This model is coupled with the corresponding building thermal zone, allowing for a detailed heat and mass transfer between pool, zone air and AHU. The characteristics of all the equipment involved are available from manufacturer, including pump properties. Occupancy data in hourly basis for a full year are available from the property, and those together with regulatory demands (in litres/person/day) are used to characterize the DHW load.

The AHU of the hall is a standard pool AHU incorporating heat recovery, enthalpy controlled free cooling and different control settings for occupancy and non-occupancy periods. This is simulated by a set of types representing coils and the rest of elements constituting the AHU (except fans, which are implemented as equations). The HP is modelled by means of a performance map approach, but the control follows the 4-stages approach of the equipment, limiting the practical available power to the real performance of the HP. The air heat exchanger has six fans in total, each one operated individually (on/off) to control the air flow at the heat exchanger.

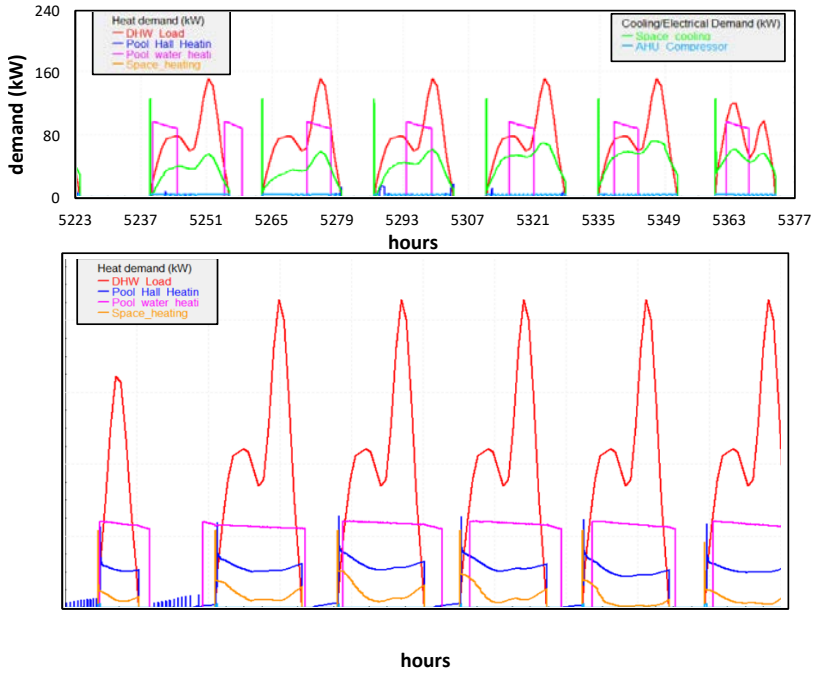

Figure 3: The sport center's thermal demands for (top) a summer week and (bottom) a winter week

In Figure 3, the heat demand variations of the sport centre and the contribution of each sub-system are presented. At the top sub-figure, the system operation for the summer week is presented. From the main pattern, the thermal needs are mostly shaped from the combination of the pool water and the DHW heat demands, while the pool hall heating is insignificant, as the summer season is generally associated with high ambient temperatures thus the heating demand is low. In addition, for the summertime period, the pool water heating, which is activated for narrow time periods each day, is significant compared to the DHW demand. However, this is not the case for the wintertime period, as it is possible to observe from the bottom sub-figure. At this period of the year, the DHW thermal demand is relatively higher compared to the pool water heat demand, which in turn is non-zero and almost steady for most hours of each day. This may be also an indication that during winter, the losses due to the lower ambient temperature are by far more significant compared to the occupational profile of the sport centre's pool, which is expected to be similar to the DHW profile. This could be also the reason that, as it can be observed from the same figure, the pool heating demand follows similar pattern to the space heating demand. Therefore, for the wintertime period, the thermal needs are mostly shaped from the DHW demand with a lower but constant contribution from the pool and space heating demands.

2.2 Heat Pump and microgrid modelling in APROS

Regarding the sport center facility in Barcelona, the thermal power production and the electrical energy system are coupled through the HP installation. Therefore, the whole energy system is integrated and the energy management of the overall plant needs to be simulated as a single unit in order to better assess any operational strategies and their impact on the system operation. Thus, the modelling of the thermal systems carried out in TRNSYS (heat demand/thermal loads) provided the boundary conditions for the detailed dynamic simulations of the HP (heat supply) and microgrid (electricity demand/supply) models of the sport center, developed in APROS. Those are described in detail below.

The HP is an electrical to thermal energy converter and therefore it is the coupling point for the simulation of the sports center electrical microgrid. The latter consists of a 25 kWp PV installation and a BESS rated at 1080 Ah/48 V/17.3 kW constant discharging power. The battery can interact with the main grid either to charge or discharge and it is operated by the EMS which implements the chosen operational strategy, as a set of rules based on logic operations. The electric power requested from the HP, which was calculated from the HP dynamic model, was augmented by the corresponding fan and AHU power consumption time series (input from TRNSYS) and used as input for the microgrid simulation in APROS. The operational strategies that were decided to be evaluated, were 1) the peak shaving of the aggregated electric demand (HP, AHU, Fans) and 2) the pricing-based battery operation (arbitrage). At this point it is important to specify that those EMS strategies were selected to be compared due to their simplicity, which makes them attractive for practical application and the grid-connected nature of the under investigation microgrid. Even though the EMS functionalities targeted at specific time intervals, their operation was autonomous and through the defined set of logic rules they were regulating the microgrid at every time instant. The continuous operation logic flowcharts are presented below (Figure 11 and Figure 15). Thus, battery charging/discharging operation and mains energy flows were constantly regulated by the corresponding EMS throughout the whole simulation period of time. The developed simulation models and the operational strategies are described in more detail in the following sections. Figure 4 depicts the overall system configuration.

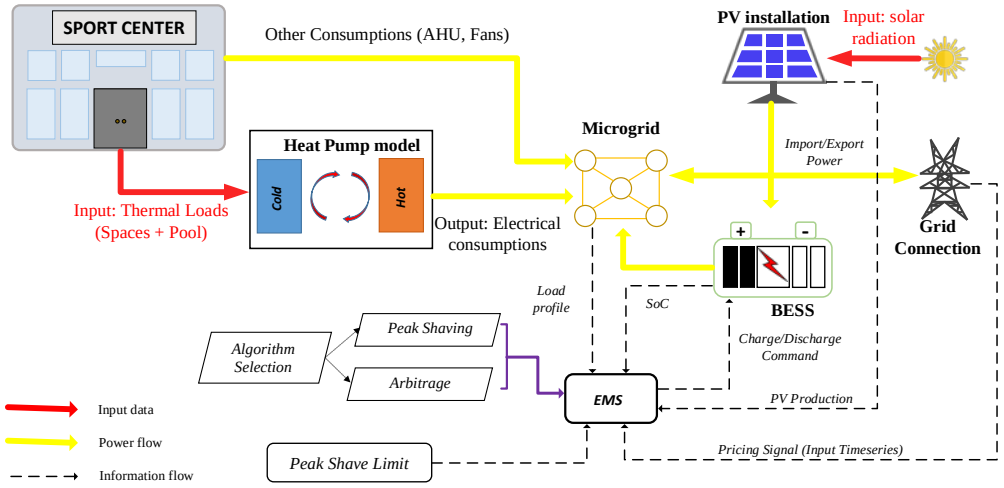

Figure 4 : Barcelona sport centre overall system simulation model.

2.2.1 Detailed heat pump dynamic modelling and simulation

As the occupation of the centre and the ambient air temperature vary, the heating demand is also changing according to this periodic variation, as shown earlier. Therefore, the heating production system, which is basically the HP, is forced to constantly alter its thermal output in order to follow the load changes and simultaneously adapt its operation according to the varying environmental conditions. Based on [16], most of the practical control approaches manipulate the refrigerant mass flow rate and evaporator pressure or temperature to regulate the system performance. Refrigerant flow rate and evaporator conditions can be adjusted using the VSC and a variable opening EEV, respectively. This allows for two degrees of freedom, and for a given operating condition of refrigerant mass flow rate (or compressor speed), there will be a unique valve position satisfying the desired evaporator conditions. Under this consideration, the following control loops were considered in the present study:

- Condenser water outlet temperature regulation through water mass flow control
- Condenser refrigerant heat output regulation through VSC control
- Constant superheating regulation at the evaporator outlet, through EEV control

A dedicated PI(D) controller was assigned for each of the above-mentioned tasks, due to the wide and timeless industrial applicability and practical implementation simplicity of this controller type.

The compressor of a HP, which is mostly responsible for the generation of the necessary refrigerant fluid mass flow is considered as the most important component for the capacity control of the HP system [29]. In order to simulate this component with the corresponding available APROS module, the compressor map was adjusted in order to best represent the design operational points given from the manufacturer. Those data refer to the HP capacity for specific environmental conditions (i.e. ambient temperature) and are presented in Table

1. The compressor map can be then used iteratively, for the calculation of the associated thermodynamic variables and the compressor power consumption based on the following procedure. At each iteration *k*, the reduced refrigerant mass flow through the compressor and the rotational speed are calculated from APROS as

$$\dot{m}_{red}^{k} = \dot{m}^{k}\sqrt{\frac{T_1^k}{T_{01}^k}}\frac{P_{01}^k}{P_1^k} \quad \text{Equation 1}$$

$$N_{red}^{k} = \frac{N^k}{N_0^k}\sqrt{\frac{T_{01}^k}{T_1^k}} \quad \text{Equation 2}$$

respectively. T_1, P_1, N_1 are the inlet temperature, inlet pressure and compressor rotational speed at the current operating point respectively, whereas T_{01}, P_{01}, N_0 are the inlet temperature, inlet pressure and compressor rotational speed at the nominal operating point respectively. Finally, $\dot{m}$ is the refrigerant mass flow through the compressor. Then the pressure ratio Π^k can be estimated from the compressor map as

$$\Pi^k = \frac{P_2^k}{P_1^k} = f_{map}\left(\dot{m}_{red}^k, N_{red}^k\right) \quad \textit{Equation 3}$$

, where the subscript 2 denotes the compressor outlet. Then the pressure ratio value is updated using a 1st order Taylor approximation, considering its dependency on the refrigerant mass flow as

$$\Pi^{k+1} = \Pi^k + \frac{\partial \Pi^k}{\partial \dot{m}^k}\left(\dot{m}^{k+1} - \dot{m}^k\right) \quad \text{Equation 4}$$

Upon convergence, the final pressure ratio value Π is used to calculate the compressor power P^c as

$$P^c = \frac{1}{\eta_{is}^c}\dot{m}C_pT_1\left(\Pi^{\frac{R}{C_p}} - 1.0\right) \quad \textit{Equation 5}$$

, where

$$R = \frac{R_0}{M}\, and\ C_p = C_p\left(\frac{T_1 + T_{2s}}{2}\right) \quad \textit{Equation } \boldsymbol{6}$$

R is the gas constant, R_0 the ideal gas constant, M is the molecular mass of the refrigerant and C_p its heat capacity, T_1 the inlet temperature and T_{2s} the isentropic outlet temperature, η_{is}^c the isentropic efficiency, Π the pressure ratio and $\dot{m}$ the mass flow.

In the current HP model, the compressor speed was controlled in order to achieve the desired heating capacity of the HP, based on the corresponding thermal load which was set as an input. This was accomplished with the use of a PI controller that was responsible for the tracking of the HP setpoint, for small deviations around its nominal value and with a feedforward action of the nominal speed ($N_0 = 3000\ rpm$)

$$N(s) = N_0 + \frac{k_{P,c}s + k_{I,c}}{s}\left(Q_{cond}^{SP}(s) - Q_{cond}^{meas}(s)\right) \quad \textit{Equation 7}$$

This control loop is implemented via an inverter that controls the compressor speed and as a result, the refrigerant mass flow is changed in order to achieve the desired heating output at the condenser. The heat flow from the condenser to the water circuit can be calculated by measuring the supply and return temperatures and the water mass flow.

The control valve was used to regulate the superheating of the evaporated refrigerant. For this purpose, a PID controller was employed and integrated into the simulation model. The control valve used in simulations was selected to have an equal percentual valve characteristic (representing the typical behavior of such system components). Thus, it is possible to estimate the pressure loss coefficient of the valve which is later used for the calculation of the pressure drop at the EEV as:

$$\Delta p = \frac{1}{2}\rho k_v(x_v)u^2 \quad \textit{Equation 8}$$

where $k_v(x_v)$ is the loss coefficient as a function of the opening percentage of the valve $0<x_v<1$ (x_v=1 corresponds to a fully open valve), ρ is the refrigerant's density and u is the fluid velocity. The superheating degree was regulated by its dedicated PID controller as

$$\Delta x_v(s) = \frac{k_{D,v}s^2 + k_{P,v}s + k_{I,v}}{s}\left(\Delta T_{SH}^{SP}(s) - \Delta T_{SH}^{meas}(s)\right) \quad \text{Equation 9}$$

where $\Delta x_v(s)$ is the change of the valve position signal, $\Delta T_{SH}^{SP}(s)$ and $\Delta T_{SH}^{meas}(s)$ the setpoint and measurement of the superheating degree signals and $k_{P,v}$, $k_{I,v}$, $k_{D,v}$ are the proportional, integral and derivative gains respectively. The EEV control loop can measure the level of superheated refrigerant vapor and actuate on the valve opening position in order to adjust the refrigerant mass flow. The ambient temperature variation is considered as a disturbance realization to the system that has an effect on the evaporating temperature, which in turn affects the condensing temperature in order to provide the specified thermal output. At this point it is remarked that due to i) the non-linear behavior of the EEV (especially away from the design point), and ii) its coupled dynamics with the other HP components as explained above, the controller was not able to appropriately regulate the superheating for low loads (<30%) and thus the valve position was kept constant for these occasions. Then, the valve position was selected such that a higher degree of superheat than the setpoint is achieved, ensuring that no liquid will enter the compressor and thus resulting in a stable system operation. This is in agreement with [17] where the authors stated that their controller had issues on performing satisfactorily away from the design operating point. In addition, despite that simple proportional-integral-derivative (PID) feedback loops are inexpensive and easy to install, their tuning for a wide range of operating conditions and ensuring their stability can be cumbersome. These issues lead to gain-scheduling and multivariable controls schemes that were not the purpose of this study. For further information about advance control structures in HPs, the reader is directed to [16].

The modelling of the condenser and evaporator parts of the HP unit was based on the heat exchanger modules of the APROS thermal components library. The heat transfer and the phase change of the refrigerant were numerically solved considering a 1-D heat exchanger model based on the finite volume approach. The heat exchanger volume is discretized in order to create a network of hydraulic and thermal nodes at which the corresponding conservation equations are solved. The homogeneous solution system of APROS, utilizing the REFPROP library [30] to accurately estimate the refrigerant properties, is based on the one-dimensional conservation equations for mass, momentum and energy.

$$\frac{\partial \rho}{\partial t} + \frac{\partial (\rho u)}{\partial z} = 0 \qquad \textit{Equation 10}$$

$$\frac{\partial \rho u}{\partial t} + \frac{\partial (\rho u^2)}{\partial z} + \frac{\partial p}{\partial z} = \rho g_z + F_w \qquad \textit{Equation 11}$$

$$\frac{\partial \rho h}{\partial t} + \frac{\partial (\rho u h)}{\partial z} = \frac{\partial p}{\partial t} + q^* \qquad \textit{Equation 12}$$

$$q_{conv} = a_{conv}(T_w - T_g) \qquad \textit{Equation 13}$$

$$a_{conv} = k_{conv} \dot{m}_g^{0.6} \qquad \textit{Equation 14}$$

The condensing heat transfer was calculated based on the Shah correlation [31] as:

$$\frac{a_{kf}}{a_f} = 1 + \frac{3.8}{Z^{0.95}} \qquad \textit{Equation 15}$$

The liquid heat transfer coefficient is calculated by using the Dittus-Boelter equation:

$$a_f = 0.023 \cdot {Re_f}^{0.8} \cdot Pr^{0.4} \cdot \frac{\lambda_f}{D} \qquad \textit{Equation 16}$$

And therefore

$$a_{kf} = a_f \left[(1-x)^{0.8} + \frac{3.8 \cdot x^{0.76} \cdot (1-x)^{0.04}}{{p^*}^{0.38}} \right] \qquad \textit{Equation 17}$$

In the above equations ρ is the refrigerant density, u the refrigerant fluid velocity, z the axis along the fluid flow (1-D analysis), g_z the acceleration of gravity, F_w the wall friction forces, h specific enthalpy of the refrigerant, p the refrigerant's pressure, q^* the external source heat flux, q_{conv} the convective heat flux, a_{conv} the convective heat flux coefficient, T_w the water temperature, T_g the refrigerant (gas) temperature, k_{conv} the increase in heat transfer coefficient, $\dot{m}_g$ the refrigerant gas phase mass flow, a_f the liquid phase heat transfer coefficient, a_{kf} the two phase heat transfer coefficient, Z the Shah's correlation parameter, Re_f the liquid phase Reynold number, Pr the Prandtl number, λ_f the liquid phase heat conductivity, D the tube's inside diameter, x the vapor quality, p^* the reduced refrigerant pressure.

The finite volume solution method is utilized to solve the resulting one-dimensional partial differential equations. These are discretized in respect to both space and time. For the space discretization the staggered grid scheme is used, which involves the computation of the fluid state variables (i.e. pressure, enthalpy etc.) in the center of each control volume, while the flow related variables (i.e. velocities) are calculated at the junction of two control volumes. For temporal discretization, implicit solution algorithms are applied in combination with an iteration procedure. During this procedure, pressure, velocities, heat flows and enthalpies are solved one after the other and, at the end, the fluid properties (i.e. density) are updated as a function of the computed pressure and enthalpy. This iteration cycle is repeated several times during one time-step until solution is converged. As an overall convergence criterion the mass error is implemented in combination with flow and heat transfer tests, which are used to check the convergence of the pressure and enthalpy. The complete simulation model and the integrated control structures of the HP are depicted in Figure 5.

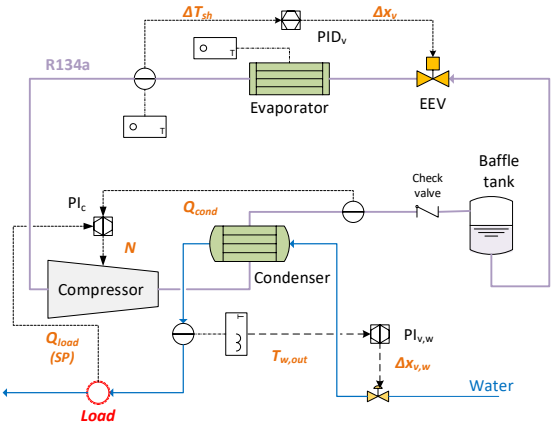

Figure 5 : Representation of the overall Heat Pump model in APROS.

The water flow at the other side of the condenser is controlled with a pressure change element (circulation pump/control valve) in order to maintain the desired water outlet temperature, which in this study is set at 45 °C. This is achieved again with a PI controller as

$$\Delta x_{v,w}(s) = \frac{k_{P,w}s + k_{I,w}}{s}\left(T_{w,out}^{SP}(s) - T_{w,out}^{meas}(s)\right) \qquad \textit{Equation 18}$$

where $\Delta x_{v,w}(s)$ is the change of the water flow regulation valve position, $k_{P,w}$ and $k_{I,w}$ are the proportional and integral gains respectively and $T_{w,out}^{SP}(s), T_{w,out}^{meas}(s)$ the outlet water temperature setpoint and measurement respectively.

For the most accurate modelling of the HP, the developed model was fine-tuned in order to best represent the HP operation at the design point, based on the available data from the manufacturer. Therefore, the model parameters were appropriately set in order to minimize the error of the predicted thermal output compared to the manufacturer's data for the various operating conditions.

Table 1: Heat Pump simulation results and validation with manufacturer data (MF).

	Q_{cond} (kW)			**Q_{evap} (kW)**			**W_{comp} (kW)**		
T_{amb}	MF	APROS	*Dev. (%)*	MF	APROS	*Dev. (%)*	MF	APROS	*Dev. (%)*
5	232.6	229.47	1.346	166.6	171.96	-3.217	66	57.51	12.864
7	244.7	244.49	0.086	178.1	183.47	-3.015	66.6	61	8.408
10	262.9	262.05	0.323	195.5	197	-0.767	67.4	65.06	3.472
15	299.2	299.3	-0.033	230.5	230	0.217	68.7	69.23	-0.771

The under-investigation HP model is the Azura-S 21.4 LT, which uses R134a refrigerant as a working medium and has a maximum heating capacity of 299 kW (heating mode). The manufacturer technical data as derived from the corresponding technical brochure along with the model predictions at the different operating points are summarized in Table 1.

After the integration of the HP process model with the corresponding controllers and their appropriate tuning in order to obtain a satisfactory dynamic HP operation, the simulation model was ready to be fed with the hourly based thermal load data provided by the TRNSYS simulations. In order to examine the heating mode operation of the HP, two different representative weeks were simulated, one for the winter (1-7/1) and one for the autumn time period (21-27/11).

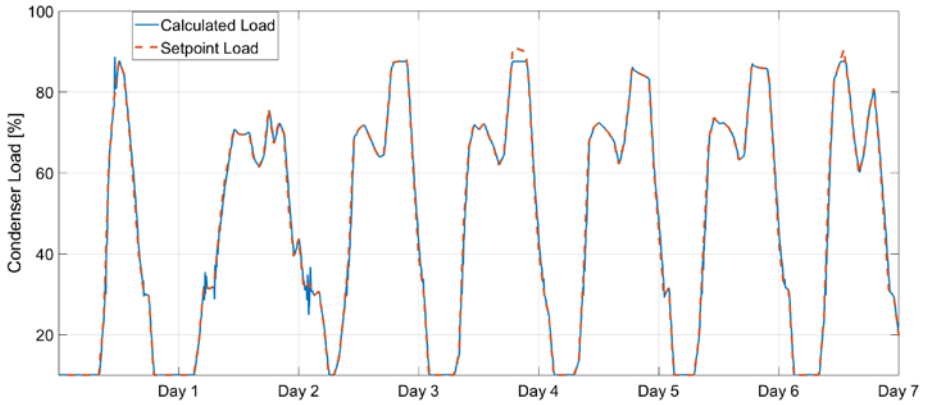

Figure 6 : Dynamic response of the controlled compressor power for the Winter week (1-7/1).

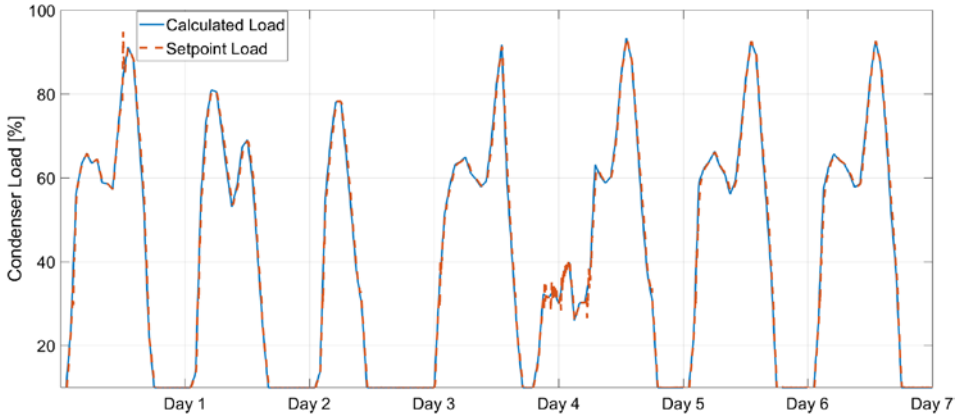

Figure 7 : Dynamic response of the controlled compressor power for the Autumn week (21-27/11).

The performance of the developed control structure of the system is depicted in Figure 6 and Figure 7 for the two simulated weeks. It is seen that the control system of the HP provides an overall satisfying performance with good tracking capability of the thermal load reference. Thus, the HP is capable for a flexible load following operation independent of each day's load pattern.

From the above simulations the corresponding power consumption of the compressor for the heating mode was calculated and compared with the simulations carried out in TRNSYS software. The results, which are depicted in Figure 8 and Figure 9, show a good agreement between the power consumption predicted from both tools, APROS and TRNSYS. The difference of the power curves predicted from the abovementioned tools can be attributed mostly to the different types of modelling. It is highlighted that the modelling procedure in APROS software is based on the thermodynamic transients regarding the temperature and the pressure variables, which derive from the numerical solution of the fluid flow and the heat transfer inside the different subcomponents of the HP system. Nevertheless, as it is seen in Figure 8 and Figure 9, the curves predicted from both tools share the same trends and a similar pattern with relatively small deviations, especially during the ramp up and the ramp down time periods.

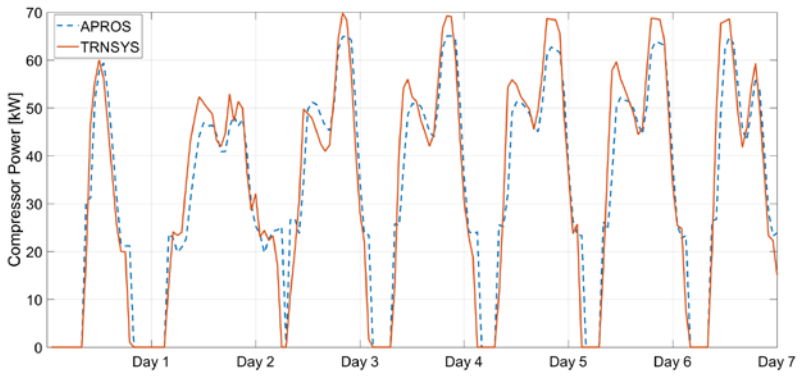

Figure 8 : Validation of the simulated heat pump operation in APROS and TRSNSYS for the Winter week (1-7/1).

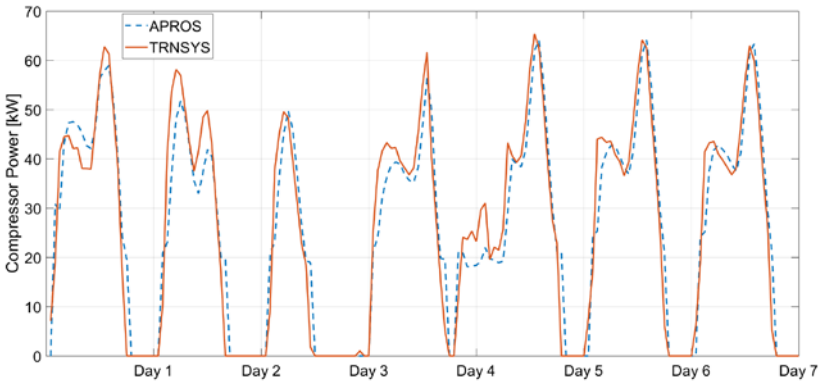

Figure 9 : Validation of the simulated heat pump operation in APROS and TRSNSYS for the Autumn week (21-27/11).

In order to further quantify the comparison of the two engineering tools regarding the compressor power consumption, the Pearson correlation coefficient between both curves and the Mean Absolute Percentage Difference (MAPD) were calculated as

$$\rho(P_A^c, P_T^c) = \frac{1}{N-1}\sum_{i=1}^{N}\left(\frac{P_{A,i}^c - \overline{P_A^c}}{\sigma_A}\right)\left(\frac{P_{T,i}^c - \overline{P_T^c}}{\sigma_T}\right) \qquad \textit{Equation 19}$$

$$MAPD(P_A^c, P_T^c) = \frac{1}{N-1}\sum_{i=1}^{N}\left|\frac{P_{A,i}^c - P_{T,i}^c}{P_{A,i}^c}\right| \qquad \textit{Equation 20}$$

where N is the number of data points of each curve, $P_{A,i}^c$ and $P_{T,i}^c$ the APROS and TRNSYS values respectively, $\overline{P_A^c}$, σ_A and $\overline{P_T^c}$, σ_T the mean values and the standard deviation of APROS and TRNSYS curves respectively.

- Winter Week (1-7/1) : $\rho(P_A^c, P_T^c) = 0.9478$ and $MAPD(P_A^c, P_T^c) = 18.71\%$
- Autumn Week (21-27/11) : $\rho(P_A^c, P_T^c) = 0.9536$ and $MAPD(P_A^c, P_T^c) = 20.67\%$

It should be highlighted that this comparison should not be considered as a regression problem where the predictions of TRNSYS must be perfectly reproduced from APROS. On the contrary, the goal was to achieve a higher fidelity and more realistic modelling of the plant (HP), through the higher level of detail offered from the latter software and check or reveal possible significant discrepancies coming from a simplified modelling. Therefore, even though deviations between the predictions from both software are reasonably expected, the general agreement of the trends (high correlation values) and the relatively low but existing differences (MAPD values not close to 0%) indicate the following:

Both types of analysis (simplified TRNSYS, detailed APROS) give similar HP performance and reveal a strong correlation between compressor power consumption and thermal demand, while the latter is mostly related to the occupation pattern of the sport center and secondly to the ambient air temperature. However, if further analysis is required where the electricity consumption of the HP is adequately estimated (as in this case), the detailed modelling approach should be followed, as this will produce more realistic results.

2.2.2 Sport centre microgrid description

In order to integrate the thermal and electrical dynamic simulation of the sport center energy system, the electrical network of the center was also modeled in APROS based on the available modules. Having completed the overall system modeling, the implementation of the different EMS algorithms with basic analog and binary modules is realized performing simulations for each operation strategy. The simulations were carried out for three representative weeks, including both of the weeks that the HP was simulated in APROS (winter and autumn time periods) and one week for the summertime period. The technical specifications of the BESS are shown in Table 2:

Table 2 : BESS technical specifications [32]

Characteristic	***Value***	***Characteristic***	***Value***
Nominal Capacity (Ah)	1080	Nominal Open Circuit Voltage (V)	48
Capacity per cell (Ah)	180	Li-ion cell VOC	3.2
SoC usage window (%)	10-90	Voltage range (V)	37.5-52.4
Nominal Energy Stored (kWh)	51.84	Maximum Charging Current (A)	-180
Cells in series (n)	15	Maximum Discharge Current (A)	360
Arrays in parallel (m)	6	Nominal Discharge Power (48 V, 360A) (kW)	17.3

At this point, it should be referred that the sport center MG facility described in this study, is one of the pilot cases of the European research project inteGRIDy [33]. Therefore, the components capacities (PV, BESS) used in this study and presented in Table 2, were selected equal to the values of the real equipment that is going to be installed at the sport center facilities and has already been defined from other studies [32]. Moreover, as the main objective of this numerical investigation is to explore the operational framework of the EMS of the existing microgrid, no special attention is paid on the impact of the appropriate sizing of the microgrid components on the overall system performance.

The complete model developed in APROS software for the simulation of the sport centre microgrid with the corresponding interconnections between the different sub modules is presented in Figure 10. The microgrid components were modelled as controlled/dependent current/voltage sources and admittances. The power converters were modeled through average power balance models with their corresponding source components. In particular, the PV installation was modelled as several PV modules connected in parallel (each of them composed of several cells) injecting current to the microgrid based on the solar irradiance level. The PV cell current source is modelled as

$$I_{sc} = \frac{G}{G_0}[I_{sc0} + k_T(T - T_0)] \qquad \text{Equation 21}$$

where I_{SC} is the short circuit cell current, G and G_0 are the actual and STC (1,000 W/m^2) solar radiances, I_{SC0} is the short circuit cell current at STC, k_T is a temperature coefficient for Isc (in A/°C), T is the cell temperature and T_0 is the cell temperature at STC (25°C). The PV's source current I_{pv} can then be determined as a function of irradiance (G) and voltage V_{pv} as

$$I_{pv} = n_{pv} I_{sc}\left[1 - C_1\left(e^{\frac{V_{pv}}{C_2 V_{oc}(T_{amb})}} - 1\right)\right] \qquad \text{Equation 22}$$

Where $V_{oc}(T_{amb})$ is the module's open circuit voltage as a function of ambient temperature, n_{pv} is the number of parallel connected modules and the coefficients C_1 and C_2 depend on the parameters of the module at standard conditions. The DC/DC converter was modelled as a controlled voltage source where, the voltage ratio was defined from a Maximum Power Point Tracking (MPPT) algorithm and the PV node voltage was appropriately set. The MPPT algorithm used in this study is the *Incremental Conductance Method* described from the following set of equations.

$$\frac{\partial P_{pv}}{\partial V_{pv}} = \frac{\partial(I_{pv} V_{pv})}{\partial V_{pv}} = I_{pv} + V_{pv}\frac{\partial I_{pv}}{\partial V_{pv}} \qquad \text{Equation 23}$$

$$\begin{cases} \dfrac{\Delta I_{pv}}{\Delta V_{pv}} + \dfrac{I_{pv}}{V_{pv}} = 0 \quad at\ MPP \\ \dfrac{\Delta I_{pv}}{\Delta V_{pv}} + \dfrac{I_{pv}}{V_{pv}} > 0 \quad left\ of\ MPP \\ \dfrac{\Delta I_{pv}}{\Delta V_{pv}} + \dfrac{I_{pv}}{V_{pv}} < 0 \quad right\ of\ MPP \end{cases}$$ Equation 24

In the APROS software, the voltage and current of the solar panel are measured after each simulation time step. The parameters ΔV_{pv} and ΔI_{pv} are calculated from two successive measurements. If the state of the panel is left of the MPP in the I-V curve, the output voltage of the MPPT is increased with a step of ΔV_{pv} and the voltage ratio of the DC/DC converter is adjusted accordingly. If the state is right of MPP in the I-V curve, the output voltage is decreased with a step of ΔV_{pv}. Basically, the PV node voltage V_{pv} is regulated from the DC/DC converter so that the injected power of the PV installation P_{pv} is maximized. Thus, from the microgrid point of view, this is considered as a current source. Further information regarding the calculation method of PV modules in APROS, can be found in [34].

The BESS is modelled as a dependent voltage source $V_{oc,Bat}(SoC)$ (based on SoC) behind a dependent resistance $R_{Bat}(SoC)$ as

$$V_{Bat}(t) = n_{Bat}V_{oc,Bat}(SoC) - \frac{n_{Bat}}{m_{Bat}}R_{Bat}(SoC)I_{Bat}$$ Equation 25

, where, n_{bat} and m_{bat} are the series and parallel Li-ion connected cells respectively. Therefore, from the microgrid's perspective, the battery is acting as a dependent current source, charging and discharging based on the DC bus voltage $V_{DC,bus}$ and its internal states (resistance and open circuit voltage) as

$$I_{Bat} = \frac{m_{Bat}\left(n_{Bat}V_{oc,Bat}(SoC) - V_{DC,bus}\right)}{n_{Bat}R_{Bat}(SoC)}$$ Equation 26

Its state of charge is updated as:

$$SoC(t) = SoC_0 - \int (I_{Bat}/C_0)dt$$ Equation 27

, where SoC_0 is the initial state of charge and C_0 the nominal capacity of the BESS. Further information about the BESS modelling can be found in [35].

The DC/AC converter connecting the sport center microgrid with the local loads (i.e. drive for the HP VSC) is modelled through a power balance equation between a DC current source and an AC controlled voltage source. The power balance between the two sides is expressed as:

$$P_L = \sqrt{3}V_{AC}I_{AC} = V_{DC}I_{DC} \Rightarrow I_{DC} = \frac{\sqrt{3}V_{AC}^2 Y_L}{V_{DC}}$$ Equation 28

where the load was modelled as a constant power load (typical for tightly speed regulated machines as the VSC and the motors for the fans) through a controlled variable admittance Y_L. The converter's DC link is regulated by an additional boost converter (current source equivalent for the DC side) taking as input the DC bus voltage $V_{DC,bus}$ (from the microgrid) and supplying the DC link with $V_{DC} \geq 1.35V_{AC}$, where V_{AC} is provided from the equivalent AC voltage source.

Finally, the interface of the microgrid with the main grid is modelled as a controlled DC voltage source (just the DC part of the interface converter). For the implementation of a controlled voltage source with power import and export capability in APROS software, two subsequent models are considered. In case of import, a controlled voltage source defines the DC bus voltage $V_{DC,bus}$ based on the EMS logic rules as depicted in Figure 11. The selected voltage level (52.4 V / 45 V / 37.5 V) is basically a function of the imbalance power and the required state of the BESS (charge, idle, discharge), as can be observed from the logic flowchart of the same figure. For modelling power export, a controllable DC load is used, acting again as a constant power load by regulating the DC bus voltage to the required value, so that the power can flow only towards the export direction.

With all the required impedances for the components of the microgrid and the sources defined, the nodal admittance matrix is created, and the power flow problem is numerically solved by APROS. For further information about the detailed modelling of the microgrid components the reader is referred to [35].

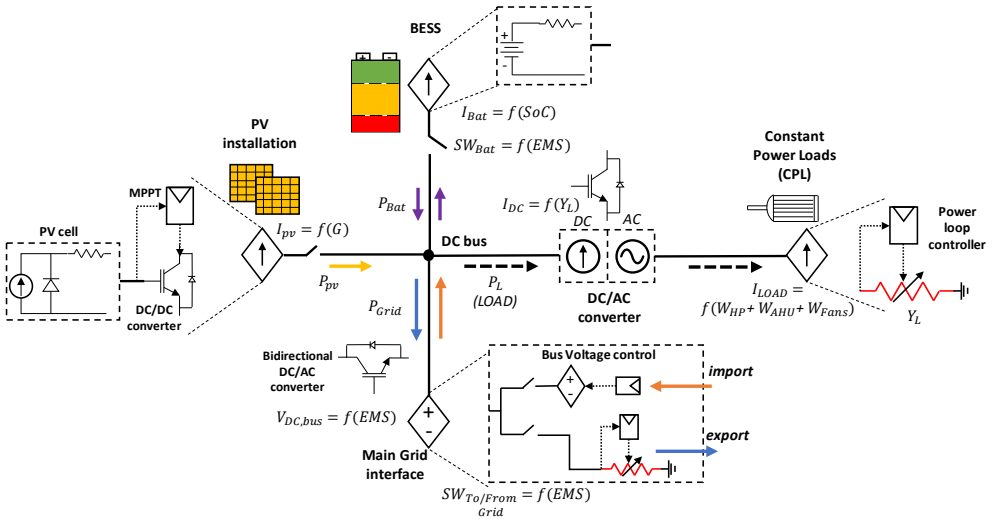

Figure 10 : Representation of the complete simulation model of the sport centre microgrid in APROS

3 Energy Management Strategies simulation

3.1 Peak Shaving Strategy results

For the peak shaving scenario, the aim was to reduce the maximum daily energy demand of the microgrid and replace it with stored energy from the BESS. This common demand response technique is mostly suitable for power systems that present a non-uniform load curve, which is particularly peaked at almost specified time periods. This may affect the cost of electricity if a demand charge scheme is in use, which is also a common case for highly demanding industrial consumers. For the Barcelona pilot case study, the pricing of the electricity was based on a continuously varying time series and therefore the demand cost was different for each time period. In addition, the combined HVAC electrical load curve presented a peak pattern which was mostly influenced by the HP electrical consumption (Figure 8 and Figure 9) and was more intense during the winter time periods. The energy management algorithm for the peak shaving scenario and its implementation into the system model developed in APROS is depicted in Figure 11.

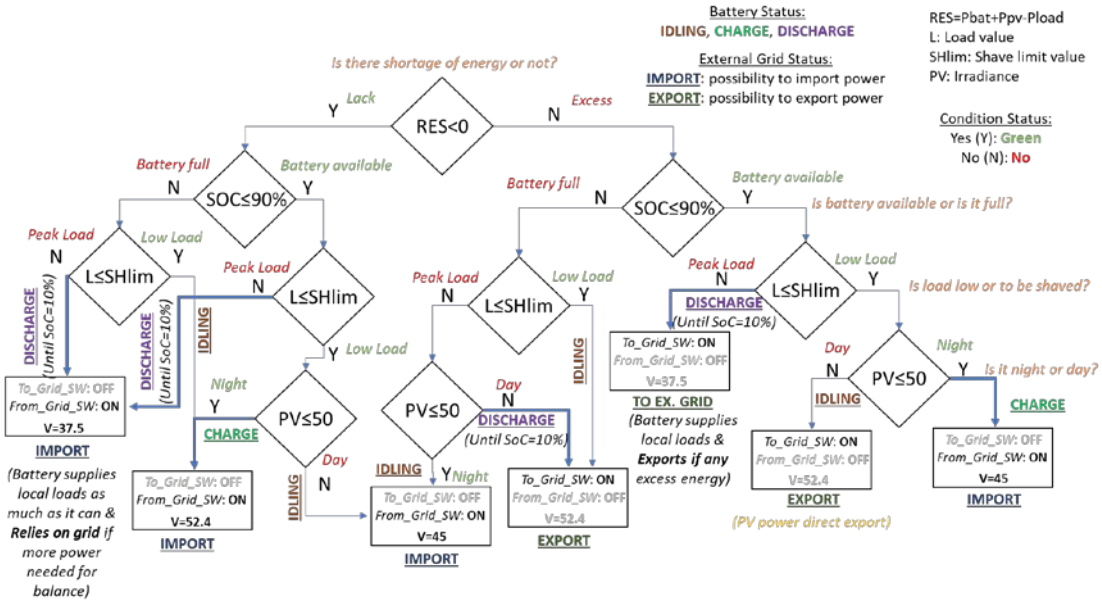

Figure 11. Peak Shaving algorithm logical diagram.

The algorithm firstly takes measurement of the current state of charge of the battery and checks if it is within the accepted operational range, which was set between 10% and 90% (Table 2). Then in case that the battery SoC is inside this range, the battery is considered as a possible source or load depending on the irradiance level and the peak shave limit. The peak shave limit is set as the 90% of each day's maximum load and this is considered as a limiter value for the power imported from the main grid. Therefore, if the load at the sport center microgrid is less than the specified shave limit value, any combination of energy supply is possible (main grid supply, BESS and PV) but if the load is greater than that value, then it should be covered from the BESS and the PV installation exclusively. Considering that the peak pattern does not always coincide with the maximum PV power production, the BESS should be able to discharge enough power to have a maximum penetration during the peak load time period. Thus, the BESS should charge only when the load is below the peak shave limit and the SoC below 90%. In this way, right before the peak load period, the BESS is at its maximum possible SoC and ready to provide its energy during the peak time period. In case that the battery is full and the load is relatively low or the battery is empty and the load is relatively high, then the battery would be disconnected and remain on idling mode, until the reverse conditions appears. At this point it is worth mentioning that the charging procedure of the BESS is decided to be during the night hours (namely when the irradiation is below 50 W/m^2) in order to avoid sudden impulses of grid power import that may exceed the shave limit value. This function is based on the fact that by visual preprocessing of the load and daylight curves, the load values at the night hours were found to be relatively lower compared to daylight time period. Consequently, for the peak shaving management system developed in this study, the BESS was charged from grid power. Figure 12 and Figure 13 present the results from the simulations for the different time periods. The variables depicted in these figures are the following:

- LOAD: Electric power demand (instantaneous power consumption from the thermal subsystem)
- P_{Grid}: The resulting power exchange between the sport center microgrid and the main grid
  P_{Grid} >0: the microgrid imports power, P_{Grid}<0 the microgrid exports power
- PV: power produced from the photovoltaic installation
- P_{Bat}: The battery (BESS) power
  P_{Bat}>0 the battery provides power (discharges), P_{Bat}<0 the battery absorbs power (charges)
- SoC: State of Charge of the BESS
- Net Load: LOAD-PV

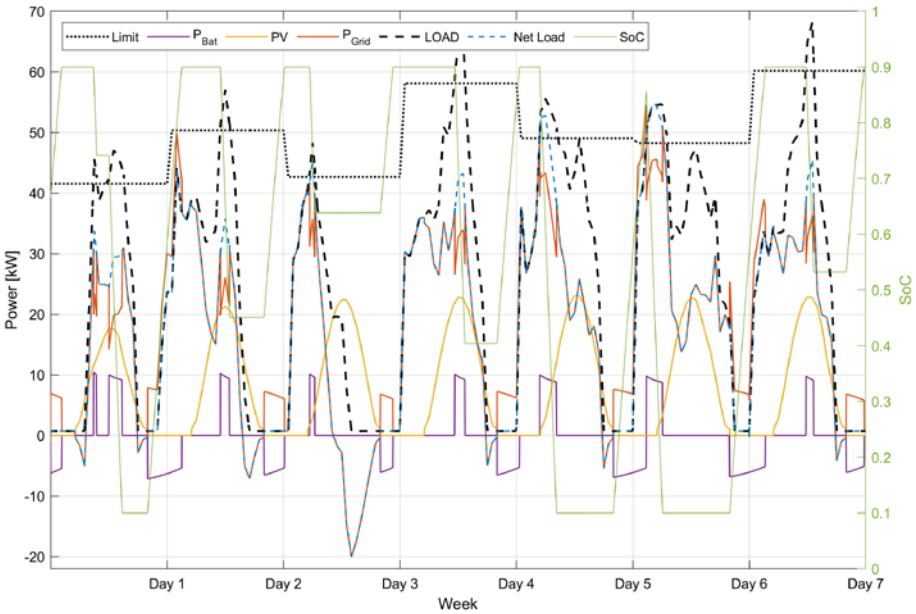

Figure 12: Peak shaving results for summer week

In Figure 12, the load is represented with a black dashed line and the corresponding peak shave limit for each hour with a black dotted line. By observing each day and the corresponding power plots it is possible to observe that the EMS manages to achieve the desired peak shaving by storing enough energy into the BESS before the peak time period occurs. This is shown from the green line (representing the battery SoC) which is on its maximum level (90% charged) for each day. Then, it starts to discharge contributing to the coverage of the

peak energy which is evident from the negative values of the magenta line (battery power). Comparing the orange line, which corresponds to the actual power exchanged with the main grid and the black dashed line of the system's load, it can be verified that the PV power generation has a significant penetration into the power system, which in turn results from the relatively high irradiation level during the summer. Thus, the PV is capable of providing around 20 kW when the maximum irradiation level is reached, which may sometimes exceed the instantaneous load consumption, as it is the case for the third consecutive day appeared in the above figure. At such cases the BESS should stay in idling mode and the excess photovoltaic energy should be exported to the main grid. This strategy is clearly evident for the aforementioned day as the high PV generation during the low load values is directly exported to the main grid (the orange curve is negative) and the battery remains on idling mode (the red curve stays flat) until the daylight is over so it can start charging back again (the green line is increasing and the power drawn from the BESS-magenta line is negative) to prepare for the next peak hours.

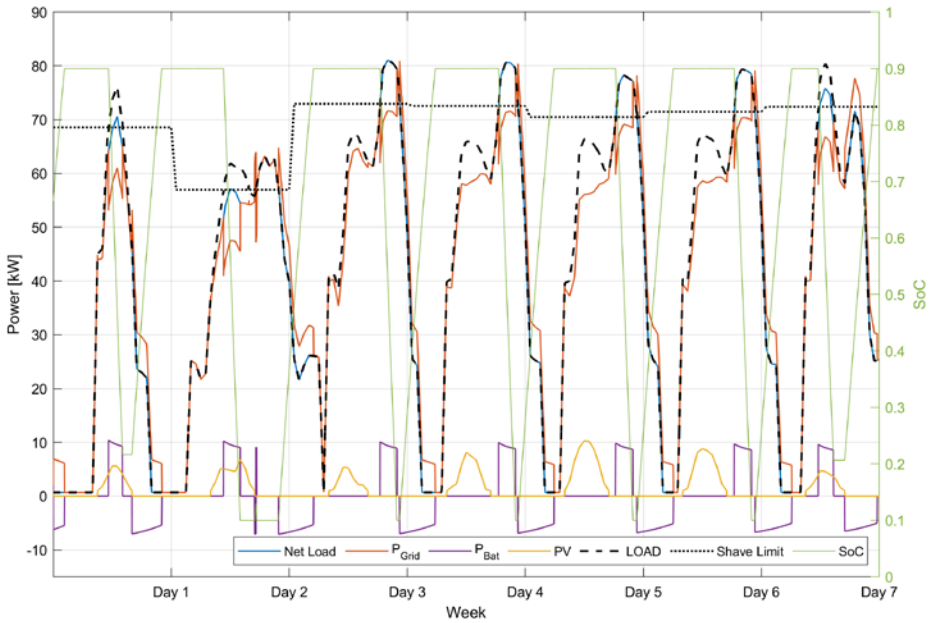

Figure 13: Peak shaving results for winter week

Following the same correspondence of colors and variables depicted in Figure 12, the same results are presented for the winter time period (1-7/1) in Figure 13. As it can be observed, the energy management algorithm is capable of shaping the load curve appropriately so that the greatest amount of the peak energy is shaved according to the set shave limit. However, the BESS provides its stored energy and it is completely discharged before the peak hour period ends, as there is not enough PV power available to cover the load. This fact combined with the night hour peak pattern appearance is the cause for the two successive smaller orange peaks that appear right after the battery is discharged. The first peak is related to the sudden impulsive power import from the grid to balance the demand as long as the battery is no further available and the second is caused by the termination of the peak hour time period which is defined from the load curve and the desired shave limit. At this case, the condition of charging the BESS is satisfied (night hours, the battery not full and the load is below the limit value) and as a result the battery starts charging from the grid with a sudden power import. This issue is associated with the relatively small capacity of the energy storage system and the decision of the peak shave limit. In order to avoid such impulsive charging conditions, the capacity of the battery should be bigger or the desired peak shaving level should be lower than the selected one. In addition, comparing the results of the summer and the wintertime periods, it is evident that during the winter week the load values are greater than the summer time period which is also accompanied by lower PV generation caused from the low irradiance. The PV power reaches a maximum of 10 kW power generation which in combination with the relatively higher load values, results in an overall lower photovoltaic penetration. The load curve during the wintertime is mostly shaped by the HP operation which is directly associated with the thermal load which in turn is maximized during the night hours.

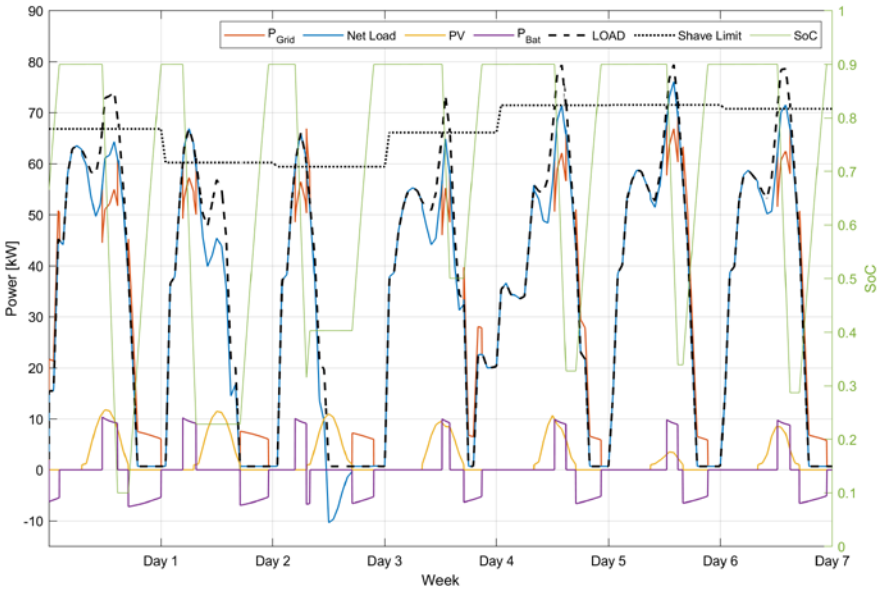

Figure 14: Peak shaving results for autumn week

Figure 14 presents the results of the simulation for the autumn time period. In this case the load values are of similar magnitude with the wintertime period and higher compared to the summertime period. However, the different day-of-week effect is remarkable during the selected week and it is depicted with the different shape and level of the load curve during the second and third day of the plot that correspond to Saturday and Sunday. As it can be easily observed from the figure above, although during this week the PV power production is around the same level as in the wintertime period, its maximization coincides with the peak hours. Consequently, in this case the sudden imports of grid power which are related to the beginning of the BESS charging period), do not violate the set peak shaving limit as also noticed in the results of Figure 12 and Figure 13. This is also enhanced by the shape of the load curve which is "pointier" at the peak hours compared to the more "rounded" winter load curve. This in turn means that during the autumn peak time periods less energy should be provided from the BESS and therefore its current capacity is sufficient. The last is also depicted by the green line of the BESS SoC which does not reach the minimum acceptable value of 10% in contrast to the wintertime period.

3.2 Pricing Based strategy (arbitrage) results

The second energy management algorithm developed and implemented in the APROS dynamic simulation was based on the provided electricity pricing signal. This pricing-based (arbitrage) scenario was focused on the economic dispatching of the storage system. In contrast to the previous energy management technique that aimed to reduce the maximum energy demand, the purpose of this strategy was to control the charging and discharging of the BESS according to the mean value of the daily cost of electricity. Thus, the battery should charge when the electricity price value was below the daily mean value in order to take advantage of the low cost and discharge when the price is above the daily mean value and a possible grid power usage is rather expensive. The algorithm is once more initiated with the state of charge measurement. In case that this is within the accepted range (10%-90%), then the pricing signal is checked and if its value is lower than the calculated mean value, then the battery charges.

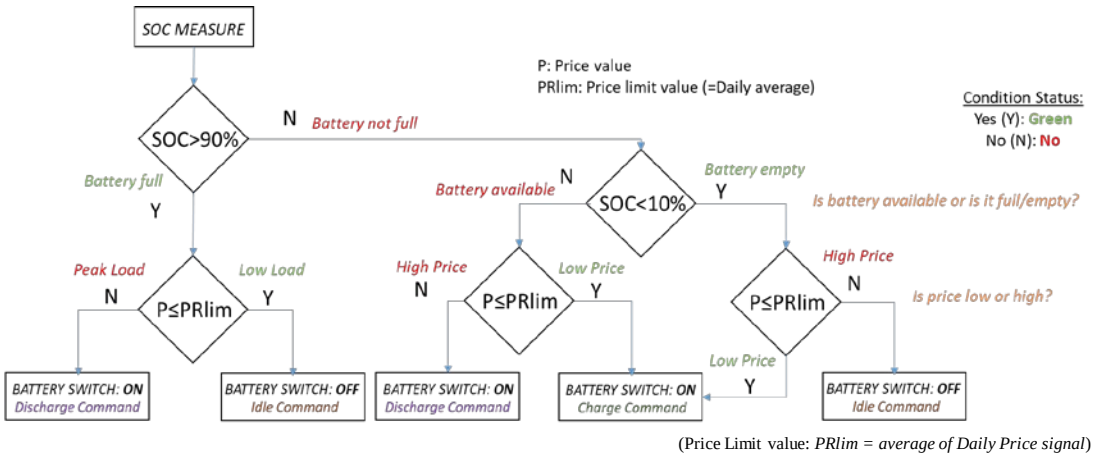

(Price Limit value: *PRlim = average of Daily Price signal*)

Figure 15. Price based algorithm logical diagram

If the opposite is true, then the battery discharges power. The same weeks that were simulated with the previous energy management algorithm were also simulated with the current management algorithm and the new cost of electricity was calculated and compared for both cases. The detailed results for the summer week are described in Figure 16 and Figure 17.

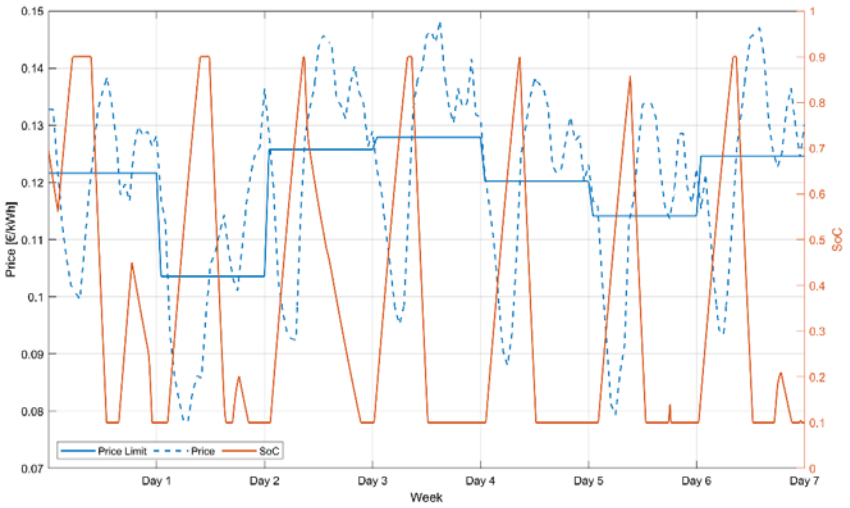

Figure 16: Pricing based results for summer week (1/2)

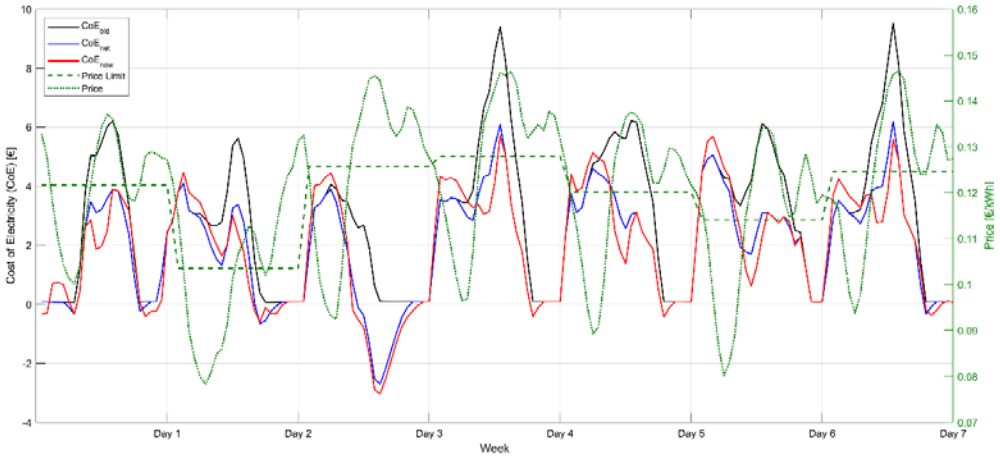

Figure 17: Pricing based results for summer week (2/2)

As it is revealed from Figure 16, the process of charging and discharging of the battery is controlled by the instantaneous pricing value and the mean daily value. This correlation is also depicted by the state of charge variation. When the pricing signal is below the mean value the SoC increases until it reaches its maximum

value (90%) and the reverse is happening for pricing values higher than the mean one. Moreover, it is possible to observe that due to the high variability of the electricity signal, in some time periods the BESS has not enough time to charge and the SoC reaches a relatively low value. This effect could have a negative impact on the health of the BESS since Li-ion cells are sensitive to the cycling patterns and power fluctuations [36]. Comparing both EMS strategies, it is noticed that generally a consistent cycling behavior pattern is followed for each of them, which is guaranteed by the battery scheduling logic, as implemented in this study. For the peak shaving strategy, the SoC fluctuations are mostly around the peak shaving periods (since the battery is in idle mode the rest of the time) whereas for the energy arbitrage case, most of the SoC variations are in correspondence with the pricing signal pattern. For this case, additional (incomplete) cycles can be identified due to the generally higher volatility of the pricing signal compared to the peak shave limit signal (Figure 13 and Figure 16 respectively). This could in turn result in higher strain of the BESS (increased cycling) which in the long term could have a higher impact on the battery's state of health. An additional effect that is also directly evident and can influence the battery's health in the long-term, is the amount of time during which the battery is kept at full and empty capacities. Generally, with the peak shaving strategy, the BESS needs to store an amount of energy for longer time periods and this may result in increased losses.

In Figure 17 the impact of the applied strategy on the instantaneous cost of electricity can be seen. First it is obvious that with the proposed algorithm the peaks of the cost of electricity signal for the net load (with PV integration) have been shifted to periods of time when the price takes lower values. Therefore, the valleys corresponding to the low-cost areas of the price signal have been greatly correlated with the peaks of the new CoE signal that are associated with areas of high grid power demand. The same trends are observed for the winter and autumn time periods (Figure 18 and Figure 19). In particular, during the wintertime period the electricity cost follows a more uniform pattern which in turn has an effect on the charging of the BESS which presents a similar pattern for most days of the week. This is a case where the shape of the cost signal allows for a maximum capacity to be reached and the battery is better used. The same principle applies also to the autumn time period which is characterized by steep changes of the pricing signal.

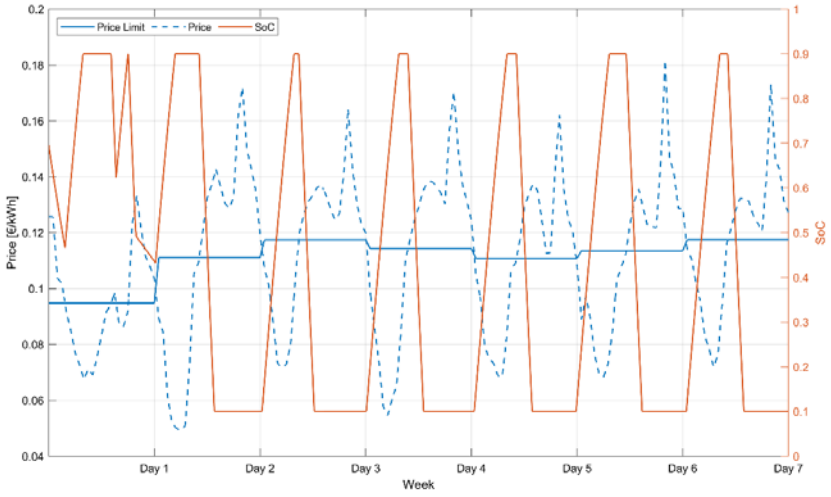

Figure 18: Pricing based results for winter week

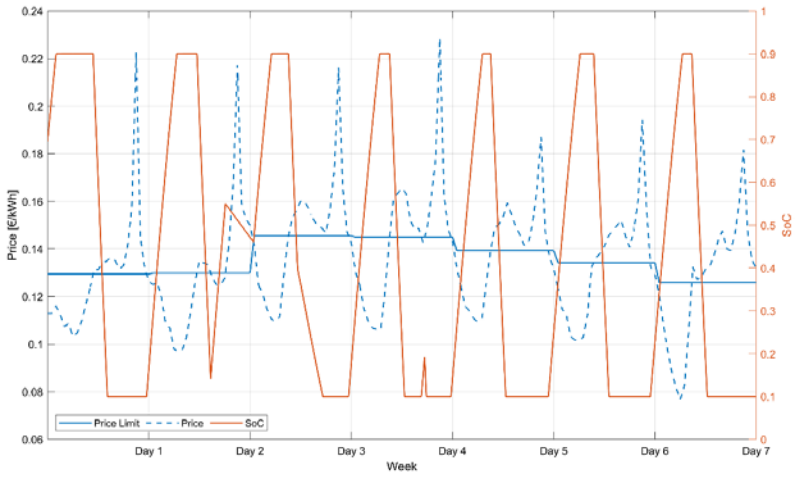

Figure 19: Pricing based results for autumn week

4 Conclusions - Discussion

The calculated costs of electricity for the simulated cases are summarized in Table 3.

Table 3 : Energy managements strategies economic assessment

Simulation Week	Base Case (€)	A. Peak Shaving EMS (€)	B. Pricing Based EMS (€)	A. (%) Reduction	B. (%) Reduction	(B-A) (%)
Summer	489.89	438.04	325.36	-10.58	-33.58	23.00
Winter	898.12	871.27	862.37	-2.99	-3.98	0.99
Autumn	767.97	732.56	717.23	-4.61	-6.61	2.00

From the calculated costs of electricity, it is revealed that the pricing-based strategy (arbitrage) is associated with lower cost of electricity for all the examined time periods. This is in accordance with the initial target of each management system as the peak shaving EMS does not take into account any economic criteria but it only considers the maximum energy demand. However, with the appropriate management of the battery to replace the peak demand energy and the available PV power, it was possible to observe a cost reduction of electricity even for this case (peak shaving EMS). This effect could be maximized especially for high power consumers which are subjected to demand charges. From Table 3, it is also clear that especially for the summer time period where the peaks of the electricity cost signal are aligned with the PV power production peaks during the daylight period, the pricing-based EMS is significantly more profitable compared to the other time periods. This is also reflected in the last column of the table above, where the relative difference of the percentage reduction of the electricity cost of the two applied strategies (A-peak shaving, B-pricing based - arbitrage) is presented. During the summer time period, at the time intervals when the cost of electricity is greater than the daily mean value, the renewable power is maximized and consequently a significant amount of energy from the grid is avoided. This effect is also enhanced by the battery storage system that replaces an additional amount of “expensive energy” with “cheaper” energy saved from a previous time period. On the contrary, during the winter and autumn time periods for which the difference of the relative savings between the two methods is much lower, the maximum PV power generation is non-coincident with the maximum cost of electricity, the latter especially for the winter period is also synchronized with the peak demand values. Thus, the peak shaving EMS has a relatively better operation compared to summer as the peak energy which is avoided from the grid happens to be simultaneously the “expensive” amount of energy, when no PV power is available and consequently the winter time period is accompanied by the lowest value of B-A indicator. Therefore, from the previous analysis it is observed that the most favorable energy management strategy highly depends on the time of the year (the amount of available renewable power), the relative temporal position of the maximum renewable generation compared to the maximum power demand and the maximum cost of electricity and most importantly whether the consumer is subjected to demand charges or not. Nevertheless, from the grid side point of view, the peak shaving of the maximum demand is directly associated with the

downsizing of the maximum power coming from conventional power generation which in turns implies lower power losses to the transmission lines, downsizing of the maximum installed capacity and possibility for better and robust power scheduling.

Acknowledgments

This work has been carried out in the framework of the European Union's Horizon 2020 research and innovation programme under grant agreement No 731268 (Integrated Smart GRID Cross-Functional Solutions for Optimized Synergetic Energy Distribution, Utilization & Storage Technologies - inteGRIDy).

5 Abbreviations

ANN: Artificial Neural Network
AHU: Air Handling Unit
BESS: Battery Energy Storage System
CoE: Cost of Electricity
COP: Coefficient Of Performance
DHW: Domestic Hot Water
GHG: Greenhouse Gas
EMS: Energy Management System
ESC: Extremum Seeking Algorithm
EEV: Electronic Expansion Valve
HP: Heat Pump
HVAC: Heating, ventilation, and air conditioning
MF: Manufacturer
MPPT: Maximum Power Point Tracking
PI: Proportional-Integral
PID: Proportional-Integral-Derivative
PV: Photovoltaic
RES: Renewable Energy Sources
SISO: Single Input –Single Output
SoC: State of Charge
TXV: Thermal Expansion Valve
VSC: Variable Speed Compressor
WT: Wind Turbine

6 Nomenclature

C_p: heat capacity, J/(kg K)
C_0: BESS nominal capacity, Ah
D: tube inside diameter, m
F: friction force per volume (N/m^3)
g: acceleration of gravity, m/s^2
G: solar irradiation, W/m^2
h: specific enthalpy, J/kg
I: current, A
V: voltage, V

k: increase of heat transfer coefficient, [-]
k_v: valve loss coefficient, [-]
$\dot{m}$: mass flow, kg/s
M: molecular mass, (g/mol)
$MAPD(P_A^c, P_T^c)$: mean absolute percentage difference
N: compressor speed (rpm)
N_{red}: reduced compressor speed for the map (rpm)
p: pressure, Pa
p^*: reduced pressure, [-]
P^c: compressor power consumption, W
P_{Bat}: BESS power, kW
P_{Grid}: Power exchange at the PCC (Point of Common Coupling), kW
Pr: Prandtl number, [-]
Q: heat, kW
q: heat flux, W/m^2
q^*: heat flow per volume, (W/m^3)
R: resistance, Ohm
Re: Reynold number, [-]
R_o: universal gas constant, J/(molK)
t: time, s
T: temperature, K
u: fluid velocity, m/s
W: work, kW
x_v: valve opening, [-]
x: vapour quality, [-]
z: coordinate value
Z: Shah's correlation parameter. [-]

Greek symbols

α: heat transfer coefficient, W/m^{2}K
Δ: difference
η_{is}^c: compressor isentropic efficiency, [-]
λ: heat conductivity, W/mK
Π: pressure ratio over the compressor, [-]
$\rho(P_A^c, P_T^c)$: Pearson correlation coeeficient
ρ: density, kg/m^3
σ: *standard deviation*

Subscripts and superscripts

amb: ambient

A: APROS

Bat: BESS

bus: bus
comp: compression
cond: condensation
conv: convenction

evap: evaporation
c: compressor
D: derivative
DC: direct current
f: liquid
g: gas
I: integral
kf: two phase
L: load
meas: measurement
oc: open circuit
P: proportional
pv: PV installation
red: reduced (compressor map)
sc: short-circuit
SH: superheat
SP: setpoint
T: TRNSYS
v: valve
w: wall
0: nominal operating point / conditions
1: compressor inlet
2: compressor outlet

7 References

[1] Eurostat. Energy, transport and environment statistics. Statistical Books, Luxembourg: Publications Office of the European Union, 2019.
[2] B.R.E.C.S.U. (BRECSU). Energy use in sports and recreation buildings. Energy Efficiency Best Practice Programme (EEBPP).
[3] E. Trianti-Stourna, K. Spyropoulou, C. Theofylaktos, K. Droutsa, C.A. Balaras, M. Santamouris, et al. Energy conservation strategies for sports centers: Part A. Sports halls. Energy and Buildings. 27 (1998) 109-22.
[4] I. Sarbu, C. Sebarchievici. Performance Evaluation of Radiator and Radiant Floor Heating Systems for an Office Room Connected to a Ground-Coupled Heat Pump2016.
[5] K. Januševičius, G. Streckienė, J. Bielskus, V. Martinaitis. Validation of Unglazed Transpired Solar Collector Assisted Air Source Heat Pump Simulation Model. Energy Procedia. 95 (2016) 167-74.
[6] V. Helpin, M. Kummert, O. Cauret. Experimental and simulation study of hybrid ground source heat pump systems with unglazed solar collectors for french office buildings2011.
[7] I. Grossi, M. Dongellini, A. Piazzi, G.L. Morini. Dynamic modelling and energy performance analysis of an innovative dual-source heat pump system. Applied Thermal Engineering. 142 (2018) 745-59.
[8] L. Fu, G. Ding, C. Zhang. Dynamic simulation of air-to-water dual-mode heat pump with screw compressor. Applied Thermal Engineering. 23 (2003) 1629-45.
[9] Z. Jin, T.M. Eikevik, P. Nekså, A. Hafner, R. Wang. Annual energy performance of R744 and R410A heat pumping systems. Applied Thermal Engineering. 117 (2017) 568-76.
[10] L. Dong, Y. Li, B. Mu, Y. Xiao. Self-optimizing control of air-source heat pump with multivariable extremum seeking. Applied Thermal Engineering. 84 (2015) 180-95.

[11] Y.S. Park, J.H. Jeong, B.H. Ahn. Heat pump control method based on direct measurement of evaporation pressure to improve energy efficiency and indoor air temperature stability at a low cooling load condition. Applied Energy. 132 (2014) 99-107.
[12] F. Liu, W. Zhu, J. Zhao. Model-based dynamic optimal control of a CO2 heat pump coupled with hot and cold thermal storages. Applied Thermal Engineering. 128 (2018) 1116-25.
[13] S.H. Lee, Y. Jeon, H.J. Chung, W. Cho, Y. Kim. Simulation-based optimization of heating and cooling seasonal performances of an air-to-air heat pump considering operating and design parameters using genetic algorithm. Applied Thermal Engineering. 144 (2018) 362-70.
[14] H. Madani, J. Claesson, P. Lundqvist. Capacity control in ground source heat pump systems: Part I: modeling and simulation. International Journal of Refrigeration. 34 (2011) 1338-47.
[15] O. Ekren, S. Sahin, Y. Isler. Comparison of different controllers for variable speed compressor and electronic expansion valve. International Journal of Refrigeration. 33 (2010) 1161-8.
[16] A. Goyal, M.A. Staedter, S. Garimella. A review of control methodologies for vapor compression and absorption heat pumps. International Journal of Refrigeration. 97 (2019) 1-20.
[17] J. Marcinichen, T. N. del Holanda, C. Melo. A Dual Siso Controller for a Vapor Compression Refrigeration System2008.
[18] L. Yang, N. Tai, C. Fan, Y. Meng. Energy regulating and fluctuation stabilizing by air source heat pump and battery energy storage system in microgrid. Renewable Energy. 95 (2016) 202-12.
[19] Y. Kim, L.K. Norford, J.L. Kirtley. Modeling and Analysis of a Variable Speed Heat Pump for Frequency Regulation Through Direct Load Control. IEEE Transactions on Power Systems. 30 (2015) 397-408.
[20] W. Stanek, T. Simla, W. Gazda. Exergetic and thermo-ecological assessment of heat pump supported by electricity from renewable sources. Renewable Energy. 131 (2019) 404-12.
[21] H. Li, P.E. Campana, S. Berretta, Y. Tan, J. Yan. Dynamic Performance of the Standalone Wind Power Driven Heat Pump. Energy Procedia. 103 (2016) 40-5.
[22] L. Schibuola, M. Scarpa, C. Tambani. Demand response management by means of heat pumps controlled via real time pricing. Energy and Buildings. 90 (2015) 15-28.
[23] W. Meesenburg, T. Ommen, B. Elmegaard. Dynamic exergoeconomic analysis of a heat pump system used for ancillary services in an integrated energy system. Energy. 152 (2018) 154-65.
[24] J. Linssen, P. Stenzel, J. Fleer. Techno-economic analysis of photovoltaic battery systems and the influence of different consumer load profiles. Applied Energy. 185 (2017) 2019-25.
[25] A. Sani Hassan, L. Cipcigan, N. Jenkins. Optimal battery storage operation for PV systems with tariff incentives. Applied Energy. 203 (2017) 422-41.
[26] M. García-Plaza, J. Eloy-García Carrasco, J. Alonso-Martínez, A. Peña Asensio. Peak shaving algorithm with dynamic minimum voltage tracking for battery storage systems in microgrid applications. Journal of Energy Storage. 20 (2018) 41-8.
[27] J.C. Solano, L. Olivieri, E. Caamaño-Martín. Assessing the potential of PV hybrid systems to cover HVAC loads in a grid-connected residential building through intelligent control. Applied Energy. 206 (2017) 249-66.
[28] A. Buonomano, F. Calise, M.D. d'Accadia, M. Vicidomini. A hybrid renewable system based on wind and solar energy coupled with an electrical storage: Dynamic simulation and economic assessment. Energy. 155 (2018) 174-89.
[29] F. Karlsson. Capacity Control for residential Heat Pump Heating Systems. 2007.
[30] B.I.H. Lemmon EW., Huber M.L., McLinden M.O., . NIST Standard Reference Database 23: Reference Fluid Thermodynamic and Transport Properties-REFPROP. National Institute of Standards and Technology, Standard Reference Data Program, Gaithersburg, 2018.
[31] R. Santa. The Analysis of Two-Phase Condensation Heat Transfer Models Based on the Comparison of the Boundary Condition2012.
[32] Kourkoumpas D. et al. D3.1: Report on LCA and LCC inventory data for the uses cases. integrated Smart GRID Cross-Functional Solutions for Optimized Synergetic Energy Distribution, Utilization & Storage Technologies (H2020 Grant Agreement Number: 731268). CERTH, available at: https://cordis.europa.eu/project/id/731268/results, 2018. p. 127.
[33] http://www.integridy.eu/.
[34] W. Zhou, H. Yang, Z. Fang. A novel model for photovoltaic array performance prediction2007.
[35] S. Chapaloglou, A. Nesiadis, P. Iliadis, K. Atsonios, N. Nikolopoulos, P. Grammelis, et al. Smart energy management algorithm for load smoothing and peak shaving based on load forecasting of an island's power system. Applied Energy. 238 (2019) 627-42.

[36] D. Ciupageanu, L. Barelli, A. Ottaviano, D. Pelosi, G. Lazaroiu. Innovative power management of hybrid energy storage systems coupled to RES plants: The Simultaneous Perturbation Stochastic Approximation approach. 2019 IEEE PES Innovative Smart Grid Technologies Europe (ISGT-Europe)2019. pp. 1-5.